Molecular Basis of Proton Motive Force Generation: Structure of Formate Dehydrogenase-N

Mika Jormakka,[1] Susanna Törnroth,[3] Bernadette Byrne,[2] So Iwata[1,2,3]*

The structure of the membrane protein formate dehydrogenase-N (Fdn-N), a major component of *Escherichia coli* nitrate respiration, has been determined at 1.6 angstroms. The structure demonstrates 11 redox centers, including molybdopterin-guanine dinucleotides, five [4Fe-4S] clusters, two heme *b* groups, and a menaquinone analog. These redox centers are aligned in a single chain, which extends almost 90 angstroms through the enzyme. The menaquinone reduction site associated with a possible proton pathway was also characterized. This structure provides critical insights into the proton motive force generation by redox loop, a common mechanism among a wide range of respiratory enzymes.

Many membrane proteins, including adenosine triphosphate–synthase and secondary transporters, are driven by the proton motive force (p.m.f. or electrochemical proton gradient) across biomembranes. It is often thought that special molecular machinery, such as a proton pump or the Q-cycle, is required to generate the p.m.f. (*1*). However, these are exceptional cases and, indeed, did not exist in the original chemiosmotic theory proposed by Mitchell (*2*). This describes the oxygen respiratory chain as a series of redox loops, where the electrons are transferred from the "out" side of the membrane to the "in" side at each respiratory complex and are cotransported back with H^+, in the form of quinol, from the "in" side to the "out" side of the membrane between the complexes. Although this idea has been modified later by adding proton pumps and the Q-cycle, the simple redox loop still seems the most common mechanism for p.m.f. generation and is used by a wide range of organisms (*3*, *4*).

Escherichia coli provides an ideal system to study the structural basis of the redox loop mechanism, which is yet to be fully explained. During the anaerobic growth of *E. coli* in the presence of nitrate, the major electron donor to the nitrate respiration system is formate, which is produced from pyruvate through acetyl–coenzyme A. In this condition, two integral membrane proteins are induced: dissimilatory nitrate reductase (Nar) (*5*) and formate dehydrogenase-N (Fdh-N, N = nitrate inducible) (*6*, *7*). Both enzymes have two membrane associated subunits (α and β) and one integral membrane subunit (γ), a common subunit composition among membrane-bound respiratory enzymes (*8*). Jones demonstrated p.m.f. generation by the Nar/Fdh-N system and has proposed a redox loop mechanism responsible for this energy conservation (Fig. 1) (*6*). However, the following two major questions remain to be answered in order to understand how the p.m.f. is generated by these enzymes. (i) Membrane topology of the menaquinone binding site in Fdh-N. Electron paramagnetic resonance (EPR) studies showed that the menaquinone binding site in Nar is in close proximity to a heme *b* on the periplasmic side (*5*). However, the side of the membrane from which protons are taken up to the Fdh-N menaquinone binding site is yet to be determined. This is a critical issue in resolving whether Fdh-N and Nar are, indeed, forming a redox loop coupled by menaquinone. (ii) Membrane topology of the Fdh-N α subunit. It is generally accepted that the α subunit of Nar exists on the cytoplasmic side (*5*). Although the Fdh-N α subunit is highly homologous to the Nar counterpart, its membrane topology is yet to be determined. This is critical to elucidate whether the electron-transfer reaction from formate to nitrate contributes to the membrane potential generation (see discussion).

Here, we present the structure of Fdh-N at 1.6 Å. A comparative study of the Fdh-N with other related respiratory enzymes, including Nar and [NiFe] hydrogenase, has successfully explained how the p.m.f. is generated by the Fdh-N/Nar system.

Overall structure. Details of sample preparation, crystallization, and structure determination are provided in the supplementary material (*8*). Statistics for data collection and structure determination are summarized in Table 1.

The overall structure of Fdh-N is shown in Fig. 2. Fdh-N is packed as a trimer (total molecular mass = 510 kD) with the monomers related by a crystallographic three-fold symmetry axis (Fig. 2, A and B). The trimer shows a "mushroom"-like shape with the largest dimensions of 125 Å (along the membrane) by 150 Å (along the membrane normal). Two observations suggest that this is a physiological trimer: (i) The monomers are very tightly packed with a contact surface of ~5254 $Å^2$, and (ii) a cardiolipin molecule, a phospholipid derived from the original *E. coli* membrane, is maintained at the trimer interface.

The crystal structure indicates that α and β subunits of Fdh-N are on the periplasmic side of the membrane (Fig. 2C). The α and β subunits exist on the opposite side of the membrane from the NH_2- and COOH-termini of the γ subunit, which have been consistently determined to be located in the cytoplasm (*9*, *10*).

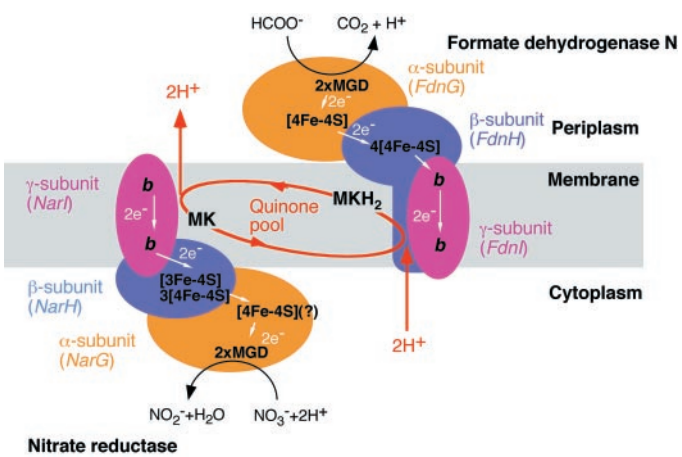

Fig. 1. A proposal for how proton motive force is generated by Fdh-N and nitrate reductase in *Escherichia coli* inner membrane. MK, menaquinone; MKH_2, reduced form of menaquinone; MGD, molybdopterin-guanine dinucleotide; *b*, heme *b*; FeS, iron-sulfur cluster.

[1]Division of Biomedical Sciences and [2]Department of Biological Sciences, Imperial College, London SW7 2AZ, UK. [3]Department of Biochemistry, BMC, Uppsala University, Box 576, S-75123 Uppsala, Sweden.

*To whom correspondence should be addressed. E-mail: s.iwata@ic.ac.uk

Electron transfer. In the Fdh-N structure, all the redox centers are aligned in a single chain, which extends almost 90 Å through the enzyme (Fig. 2C). Through the chain, electrons can be transferred from formate in the α subunit to menaquinone (HQNO in the structure) in the γ subunit. In the catalytic site, the Mo directly takes up electrons from the bound substrate (*11*). These electrons are transferred to the β subunit though the [4Fe4S] cluster (FeS-0) in the α subunit. The four [4Fe-4S] clusters in the β subunit, which are aligned in the order of FeS-1, FeS-4, FeS-2, and FeS-3, connect the α and γ subunits like an "electric wire." From FeS-3 of the β subunit, electrons are transferred to heme b_P (P for periplasm) in the γ subunit and then across the membrane to heme b_C (C for cytoplasm). Menaquinone binds to a histidine ligand ($His^{\gamma 169}$) of heme b_C and can directly accept electrons through this residue. The electron transfer from formate (standard redox potential, −420 mV) to menaquinone (−75 mV) is a highly exergonic reaction, allowing the electron transfer against the membrane potential.

Edge-to-edge distances between the redox centers are in the range of 6.0 Å [molybdopterin-guanine dinucleotide (MGD) to FeS-0] to 10.7 Å (heme b_P to heme b_C), which is shorter than the reported limit (14 Å) for physiological electron transfer (*12*). However, the shortest distance between metal centers in different monomers is 26.5 Å (edge to edge for FeS-3 clusters), which indicates that electron transfer only occurs within the monomer.

The existence of an FeS-0 cluster in the α subunit of Nar has been questioned because one of the four cysteine residues for the potential cluster binding is replaced by a histidine residue and the cluster has not been detected by EPR (*13*). In the Fdh-N structure, edge-to-edge distance between MGD and FeS-1 in the β subunit is 12.0 Å. This is within the limit of physiological electron transfer and suggests that direct electron transfer between MGD and FeS-1 is possible without FeS-0.

α subunit and formate oxidation site. X-ray structures are available for a number of soluble MGD enzymes (*14*) related to the α subunits of Fdh-N and Nar, including dimethyl sulfoxide (DMSO)–reductase (*15*), periplasmic nitrate reductase (*16*), and Fdh-H (*11*), a component of the anaerobic formate hydrogenlyase complex of *E. coli*. The structure of Fdh-H revealed that the molybdenum is directly coordinated to the selenium and both MGD cofactors.

The α subunit of Fdh-N (982 residues) is considerably larger than that of Fdh-H (715 residues), containing an extra sequence not present in Fdh-H. The core structure of Fdh-N is, however, similar to the Fdh-H structure. The two enzyme structures can be superimposed with a root mean square (r.m.s.) deviation of 1.9 Å for 599 Cα atoms with the program O (*17*). The α subunit of Fdh-N is composed of five domains, organized around the MGD cofactors (Fig. 3, A and B). Four (I to IV) of them are similar to the domains of Fdh-H, whereas one domain, which is inserted between domains III and IV, does not exist in the Fdh-H structure. We have designated this domain as domain V.

Domain I is the [4Fe-4S] cluster binding domain. The formate oxidation site is situated at the bottom of the cleft formed between domains II and III (Fig. 3, A and C). Because the crystals were obtained from the naturally oxidized protein, this crystal structure most likely represents the oxidized form with a Mo(VI) atom. The molybdenum is coordinated by two *cis*-thiolate groups from each of the MGD cofactors, the selenate group of $SeCys^{\alpha 196}$, and a hydroxide ion (w48). The ligands have a triangular prism coordination pattern; one triangular face is composed of S12 of MGD2, S13 of MGD1, and Seγ of $SeCys^{\alpha 196}$ and the other is composed of S12 of MGD1, S13 of MGD2, and O of w64 (Fig. 3B). The average distance between Mo and S atoms is 2.3 Å, whereas the distances between Mo to Se and Mo to O atoms are 2.6

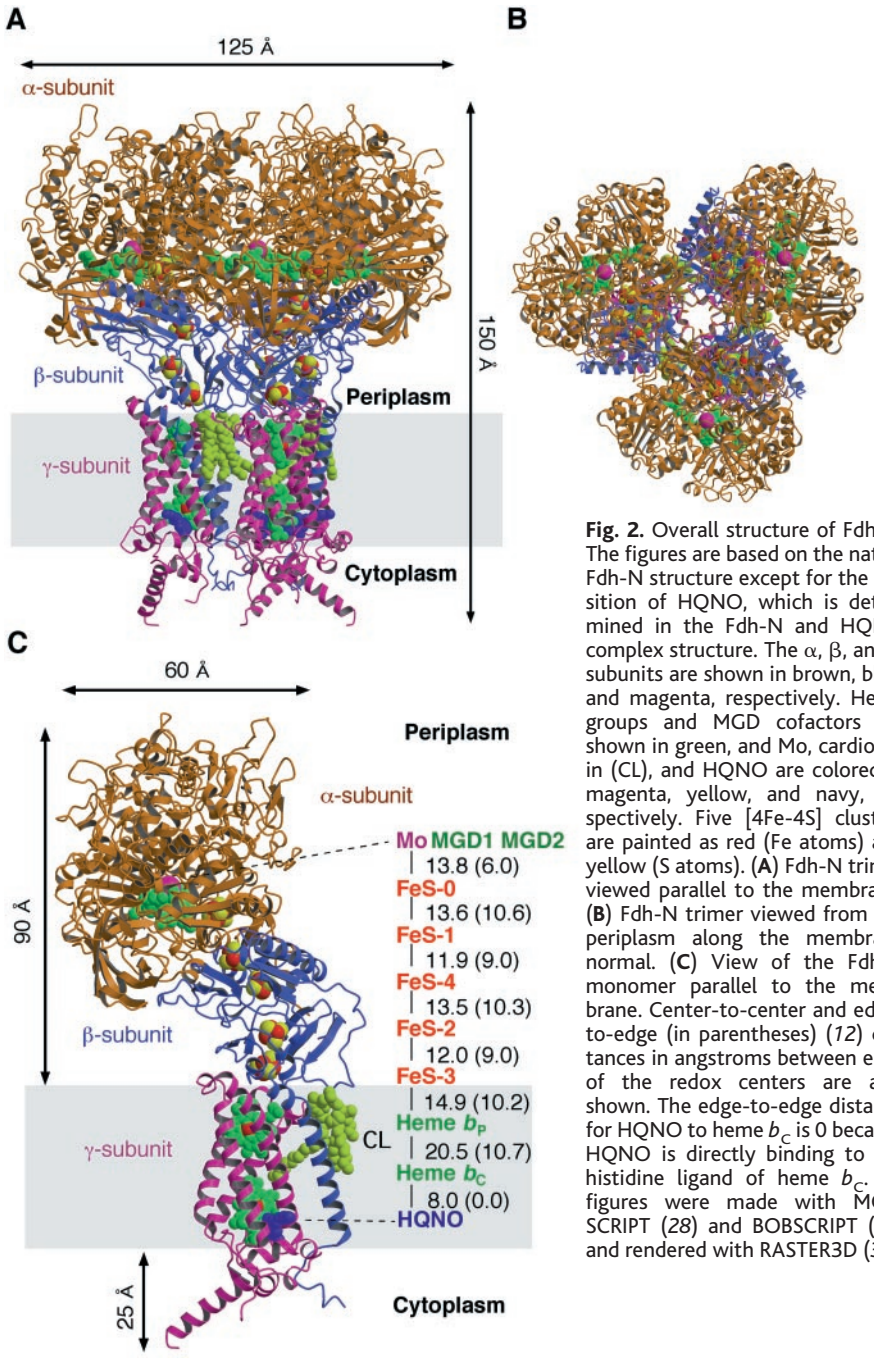

Fig. 2. Overall structure of Fdh-N. The figures are based on the native Fdh-N structure except for the position of HQNO, which is determined in the Fdh-N and HQNO complex structure. The α, β, and γ subunits are shown in brown, blue, and magenta, respectively. Heme groups and MGD cofactors are shown in green, and Mo, cardiolipin (CL), and HQNO are colored in magenta, yellow, and navy, respectively. Five [4Fe-4S] clusters are painted as red (Fe atoms) and yellow (S atoms). (**A**) Fdh-N trimer viewed parallel to the membrane. (**B**) Fdh-N trimer viewed from the periplasm along the membrane normal. (**C**) View of the Fdh-N monomer parallel to the membrane. Center-to-center and edge-to-edge (in parentheses) (*12*) distances in angstroms between each of the redox centers are also shown. The edge-to-edge distance for HQNO to heme b_C is 0 because HQNO is directly binding to the histidine ligand of heme b_C. All figures were made with MOLSCRIPT (*28*) and BOBSCRIPT (*29*) and rendered with RASTER3D (*30*).

and 2.2 Å, respectively. The Mo to O distance indicates that the ligand is not an oxo group (O=), but a hydroxide group (OH^-).

When the structure of the Fdh-H inhibitor-NO_2^- complex [Protein Data Bank (PDB) entry 1FDI] is superimposed onto the Fdh-N structure, the NO_2^- is placed on the Mo ligand w48 and w630, which is hydrogen-bonded to w949 and $His^{\alpha 197}$ (Fig. 3B). The imidazole ring of $His^{\alpha 197}$ in Fdh-N structure is rotated by 180° around the C_β-C_γ bond compared with the equivalent residue in the Fdh-H model. This is shown in the Fdh-N structure because of the hydrogen bond between $His^{\alpha 197}$ $N_{\delta 1}$ and w949. Therefore, in the Fdh-N structure, $N_{\delta 1}$ atom of $His^{\alpha 197}$ should be in close proximity to the formate α-proton, which can be modeled from the superimposed NO_2^- position. This supports the direct involvement of $His^{\alpha 197}$ in the α-proton removal as proposed in an EPR study (*18*) rather than the mechanism proposed for the Fdh-H structure, where $SeCys^{\alpha 196}$ is involved in the α-proton removal (*11*).

Domain V is not conserved among the MGD enzymes and is not present in Fdh-H. This domain is composed of many short β strands and forms surfaces toward both the outer membrane and the trimer interface (Fig. 3, A and C). In the middle of domain V, there is a hole connected to the cleft, composed by domains II and III, which has the formate binding site at the bottom. The hole and cleft form a connected channel containing many positively charged residues, which seem to be important for the attraction of substrate (Fig. 3C). In the structure, the channel is occupied with many solvent molecules, including one HEPES (anionic buffer molecule) at the center of the hole in domain V. It is possible that this hole acts as a binding site for a yet to be identified regulatory molecule.

β subunit. The β subunit consists of an extrinsic domain with four [4Fe-4S] clusters and a COOH-terminal section including tm^β (tm for transmembrane helix) (Fig. 4A). The extrinsic domain can be subdivided into an NH_2-terminal extended structure, the core region, and a linker region. The core region of the extrinsic domain belongs to a superfamily of four FeS cluster binding domains found in many membrane-bound oxidoreductases including formate dehydrogenase, formate hydrogenlyase, nitrate reductase, [NiFe] hydrogenase, DMSO reductase, and thiosulfate reductase (*9*). The region has four sections, which repeat the common motif for [4Fe-4S] cluster binding ($CxxCxxCx_nCP$) or its slight variants as seen in sections 1 and 3 (Fig. 4B). These four sections compose two subdomains, subdomain 1 (sections 1 and 4) and subdomain 2 (sections 2 and 3), which are unexpectedly related by an approximate twofold symmetry (Fig. 4, A and B). Subdomains 1 and 2, each containing two [4Fe-4S] clusters, are superimposed with an rms deviation of 1.9 Å for 56 Cα atoms with the program O (*17*).

The coordination pattern of the FeS clusters in Fdh-N is the same as predicted for Nar by mutation analysis (*5*, *13*). Each subdomain has a similar fold to 2[4Fe-4S] type ferredoxin, which has a local twofold symmetry between two [4Fe-4S] clusters (*19*). It should be noted that the 2[4Fe-4S] ferredoxin fold of subdomain 1 is composed of two discontinuous strands of polypeptide. The four FeS clusters in the β subunit can be classified into two groups depending on their environment (Fig. 4B). The FeS-1 and FeS-3 are placed

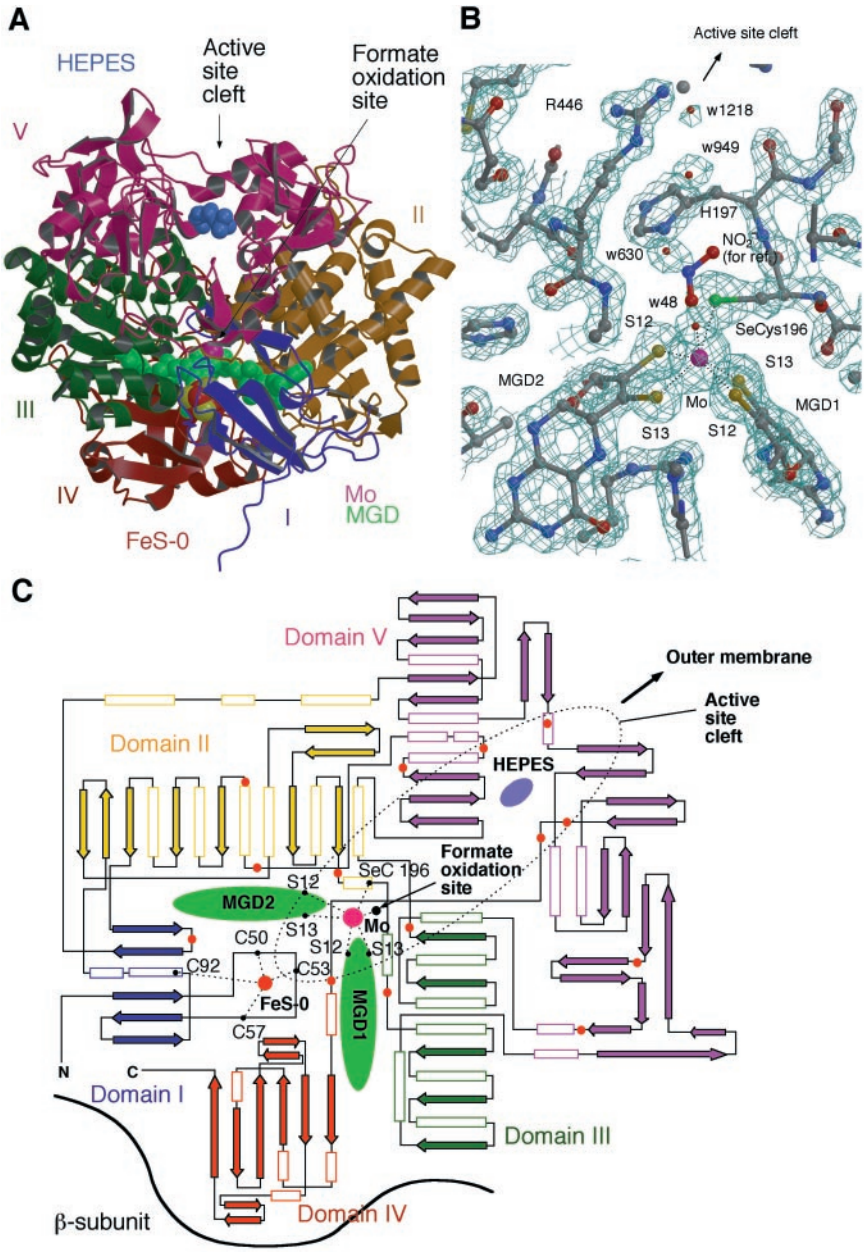

Fig. 3. Structure of the α subunit. (**A**) Ribbon representation of the α subunit. The five domains are color-coded in blue (I), yellow (II), green (III), red (IV), and magenta (V), respectively. The Mo atom and MGD cofactors are shown in magenta and green, respectively, whereas the Hepes molecule is colored in blue. The iron-sulfur cluster is shown in red (Fe atoms) and yellow (S atoms). (**B**) $2|F_o| - |F_c|$ electron density map and atomic model around the formate oxidation site. The position of an inhibitor NO_2^-, which was observed in the Fdh-H structure (PDB entry 2FDI), has been superimposed for reference. The map was contoured at 1σ. (**C**) Secondary structure schematic of the α subunit. Domains I to V are color-coded as in (A). For clarity, only the secondary structures, which are discussed in the main text, are labeled. Assignment of secondary structural elements is provided in the supplementary material (*8*). The dotted ellipsoid represents an approximate position of the active site cleft shown in (A). Red dots are the position of positively charged residues in the active site cleft and the surroundings.

close to the surface, and FeS-2 and FeS-4 are buried within the extrinsic domain. The FeS-1 and FeS-3 have hydrogen bonds only to the main-chain amide groups, whereas the FeS-2 and FeS-4 are hydrogen bonded by several positively charged residues, which could modulate the redox potentials of the clusters. This could be related to the observed large variation of redox potentials between the four FeS clusters in Nar β subunit (*20*). In Nar, two clusters, which are equivalent to surface clusters FeS-1 and FeS-3 of Fdh-N, have very high redox potentials (130 mV and 180 mV, respectively), and the other two, which are equivalent to the buried FeS-2 and FeS-4 of Fdh-N, have very low potentials (−420 mV and −55 mV, respectively).

γ subunit. The γ subunit is a membrane-bound cytochrome b with four transmembrane helices (Fig. 5, A and B). It contains two heme *b* groups and a menaquinone reduction site. [NiFe] hydrogenase and thiosulfate reductase also have a homologous cytochrome b subunit (*9*). The γ subunit forms a tightly packed trimer together with tm^{β} and one cardiolipin molecule. The 1,3-phosphoglycerol moiety of the cardiolipin is hydrogen bonded to $Asn^{\beta 15}$ and $Ser^{\beta 16}$ in the NH_2-terminal extended structure of the β subunit

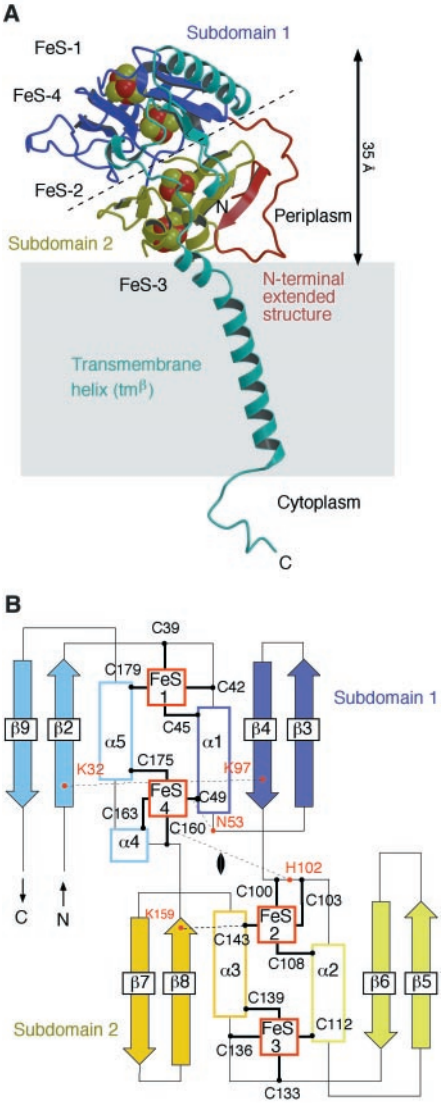

Fig. 4. Structure of the β subunit. (**A**) Ribbon representation of the β subunit viewed parallel to the membrane. An approximate twofold axis between the two subdomains is indicated by the dotted line. The NH_2-terminal extended structure, core-region subdomain 1, core-region subdomain 2, and transmembrane helix (including a linker region) are shown in red, blue, yellow, and cyan, respectively. (**B**) Secondary structure schematic of the subdomains 1 and 2 of the β subunit core region. α helices are numbered from α1 to α5, and β strands are numbered from β2 to β9. The subdomains 1 and 2 are shown in blue and yellow, respectively. The approximate twofold axis between the subdomains is also shown. Subdomains 1 and 2 are composed of sections 1 and 4 and sections 2 and 3, respectively. Sections 1 and 3 are shown in darker colors than sections 2 and 4. A, Ala; E, Glu; G, Gly; H, His; M, Met; N, Asn; Q, Gln; Y, Tyr.

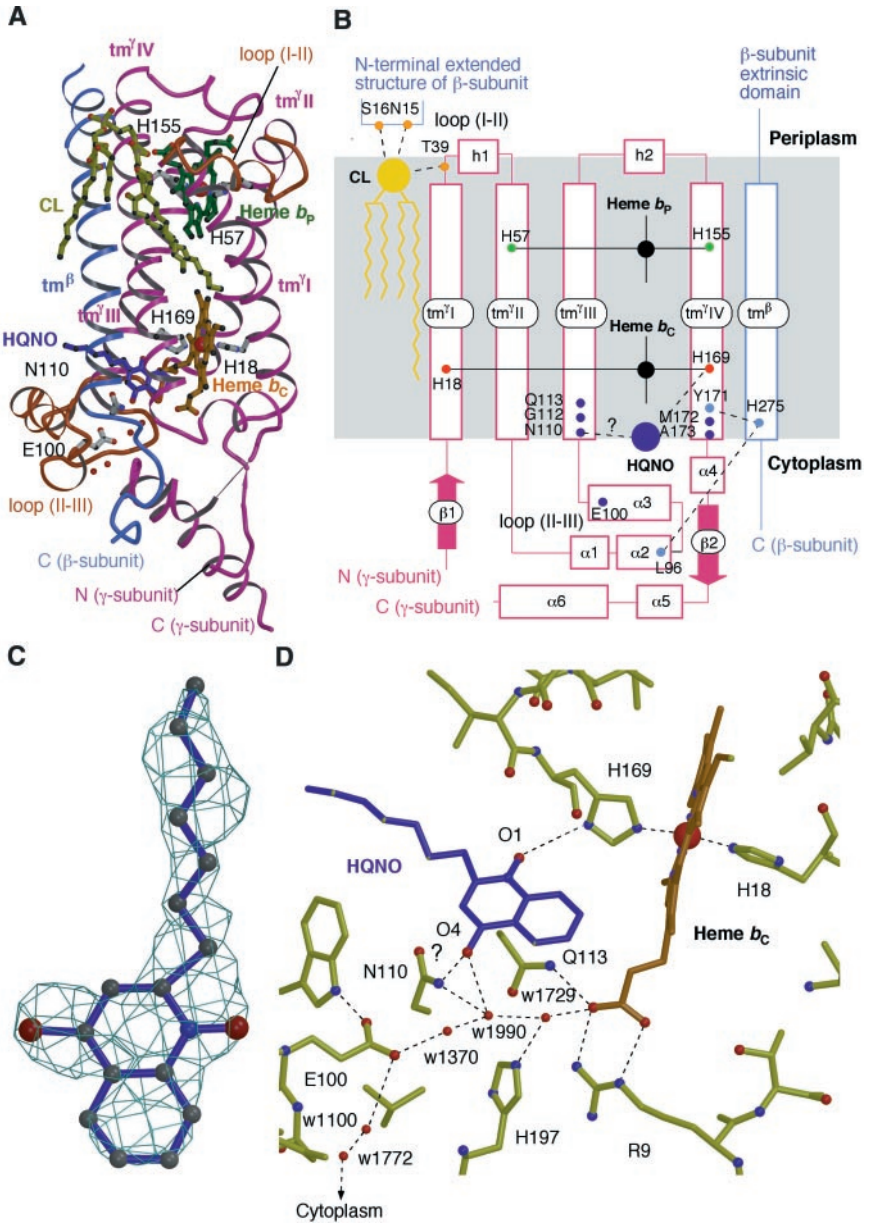

Fig. 5. Structure of the integral membrane domain. (**A**) View parallel to the membrane. Transmembrane helices for the γ subunit are numbered from tm^{γ} I to tm^{γ} IV, and the one for the β-subunit is labeled as tm^{β}. Residues involved in the bindings of two heme *b* groups and HQNO are also shown. Red dots are water molecules in a possible proton pathway from the cytoplasm to the menaquinone binding site. (**B**) Secondary structure schematic of the membrane domain. The residues involved in heme b_P, heme b_C, HQNO, and cardiolipin (CL) binding are shown in green, red, navy, and orange, respectively. (**C**) $|F_o|-|F_c|$ electron density map and an atomic model of HQNO in the menaquinone binding site. The map was contoured at 3.0 σ. (**D**) Menaquinone binding site and water molecules in a possible proton pathway.

and to Thr$^{\gamma 39}$ in the loop (I-II) of γ subunit (Fig. 5B). Lipid acyl groups mainly interact with the tm$^{\beta}$ and tm$^{\gamma}$ IV of the γ subunit of one monomer and tm$^{\gamma}$ I of the neighboring monomer. The cardiolipin molecule seems essential for the trimer formation.

Tm$^{\beta}$ and tm$^{\gamma}$ IV are tightly packed. Although most of the interactions between these helices are hydrophobic interactions, some hydrogen bonds are also observed. His$^{\beta 275}$ of tm$^{\beta}$ forms a hydrogen bond to the O_{η} atom of Tyr$^{\gamma 171}$ of tm$^{\gamma}$ IV and to the main-chain carbonyl oxygen of Leu$^{\gamma 96}$ of α2 of the γ subunit (Fig. 5B). These hydrogen bonds seem essential for stabilizing the association of the β and γ subunits. Both His$^{\beta 275}$ and Tyr$^{\gamma 171}$ are conserved for formate dehydrogenases and [NiFe] hydrogenase (*9*), and the replacement of the His$^{\beta 275}$ equivalent residue in [NiFe] hydrogenase from *Wolinella succinogenes* results in the loss of enzymatic activity (*21*).

Although all four transmembrane helices of the γ subunit are involved in maintaining the two heme *b* groups, only three helices provide the heme ligands. Heme b_P, which is on the periplasmic side and receives electrons from the β subunit, is coordinated by His$^{\gamma 57}$ of tm$^{\gamma}$ II and His$^{\gamma 155}$ of tm$^{\gamma}$ IV, whereas heme b_C, which is on the cytoplasmic side and transfers electrons to menaquinone, is coordinated by His$^{\gamma 18}$ of tm$^{\gamma}$ I and His$^{\gamma 169}$ of tm$^{\gamma}$ IV (Fig. 5, A and B). The coordination pattern is the same as predicted for [NiFe] hydrogenases (*21*, *22*). The midpoint potentials of two heme *b* groups of the *W. succinogenes* formate dehydrogenase have been measured as −20 mV and −190 mV (*23*). In the presence of a menasemiquinone analog, NQNO (2-*n*-nonyl-4-hydroxyquinoline *N*-oxide), the potential of the latter heme *b* group shifts to −230 mV; therefore, this could represent the redox potential of heme b_C.

To date, structures of two other integral membrane cytochrome b subunits have been determined; one in the cytochrome bc_1 complex (*24*) and another in fumarate reductase (*25*). Including the heme coordination pattern, the Fdh-N γ subunit structure is totally different from either, although all the cytochrome b subunits adopt a four-helix bundle for heme binding. In the cytochrome bc_1 complex, all the heme ligands are provided by two helices, whereas all four heme ligands of fumarate reductase from *W. succinogenes* belong to different helices.

Quinone reduction mechanism. The menaquinone binding site was characterized with HQNO, an analog of menasemiquinone. The structure of the Fdh-N-HQNO complex was determined at 2.8 Å resolution (Fig. 5C). The HQNO binding pocket is on the cytoplasmic side of the membrane and formed by residues from tm$^{\gamma}$ II and tm$^{\gamma}$ III and loop (II-III), which contains three short helices (Fig. 5, A and B). Residues His$^{\gamma 169}$, Asn$^{\gamma 110}$, Gly$^{\gamma 112}$, Gln$^{\gamma 113}$, Met$^{\gamma 172}$, and Ala$^{\gamma 173}$ and the porphyrin ring of heme b_C are in van der Waals contact with the hydroxyquinoline *N*-oxide ring. The *N*-oxide group of HQNO (homologous to O_1 of menaquinone) accepts a hydrogen bond from His$^{\gamma 169}$, a heme b_C ligand. In this example, the heme ligand is directly involved in quinone binding. The ligand for the OH group of HQNO (homologous to O_4 of menaquinone) is less clear; in the structure, a water molecule w1990 seems to be a direct ligand. Another possibility is the N_{ε} atom of Asn$^{\gamma 110}$, which is only 3.5 Å away from the OH group, although the CO-N angle (85°) is not suitable for a stable hydrogen bond. In *W. succinogenes* [NiFe] hydrogenase, a mutant of the equivalent residue to Asn$^{\gamma 110}$ (Asn^{128} → Asp) shows less than 10% quinone reduction activity compared with the wild type (*26*).

The w1990 is connected to the cytoplasmic space through a water chain (Fig. 5D). The water molecules are maintained by hydrogen bonds to polar residues including Glu$^{\gamma 100}$ and His$^{\gamma 19\Omega}$ and a heme b_C propionate. This seems to be a proton pathway to the menaquinone binding site. In the presence of HQNO, there is no direct connection from His$^{\gamma 169}$ to the solvent. However, in the native structure, the menaquinone binding site is replaced by solvent molecules and the water channel extends to His$^{\gamma 169}$ (*27*).

Assuming that the binding site of menaquinone is the same as that for HQNO, it is possible to explain the menaquinone reduction mechanism of Fdh-N as follows (Fig. 5D). (i) A menaquinone molecule binds to the site from the membrane. The O_1 atom of menaquinone accepts a hydrogen bond from His$^{\gamma 169}$, and the water channel connects the O_4 atom of menaquinone to the cytoplasmic space. (ii) The first electron is transferred to menaquinone. To neutralize the charge, a proton is taken up from the cytoplasmic space to the O_4 atom of menaquinone and menasemiquinone is formed. This structure should be very similar to the HQNO complex structure. (iii) The second electron is transferred and menasemiquinone is reduced to menaquinol. A proton should be taken up from the cytoplasm to Glu $^{\gamma 100}$ or to a heme b_C propionate to neutralize the charge but cannot reach the O_1 atom of menaquinol because of

Table 1. Data collection, refinement, and phasing statistic for Fdh-N structure determination.

Data set	Data collection and phasing				
	Inflection	Peak	Remote	High resolution	HQNO complex
Wavelength (Å)	1.7415	1.7382	0.9150	0.9333	0.9150
Resolution (Å)	40.0–2.5	40.0–2.5	40.0–2.5	40.0–1.6	40.0–2.8
Total observation	503,809	431,166	450,882	909,888	159,443
Unique reflections	95,911	93,876	93,929	342,711	61,817
Completeness (%)*	100.0 (100.0)	97.2 (84.7)	97.6 (87.6)	94.9 (93.3)	90.8 (74.9)
Redundancy	5.3	4.8	4.6	2.7	2.6
R_{sym} (%)*†	7.7 (18.6)	7.4 (16.3)	7.3 (24.7)	8.0 (72.2‡)	8.8 (20.9)
Phasing power§	0.85	0.76	–	–	–

Data set	Refinement‖	
	High resolution	HQNO complex
Resolution (Å)*	40.0–1.6 (1.60–1.66)	40.0–2.8 (2.80–2.90)
R factor (%)*¶	17.7 (29.4‡)	19.8 (34.4)
R_{free} (%)*#	19.5 (32.6‡)	23.9 (35.3)
Average B values	26.3	37.1
Rms deviations from ideal values		
Bond length (Å)	0.007	0.014
Bond angles (°)	1.5	3.2
Dihedral angles (°)	22.9	23.7
Improper torsion angles (°)	2.8	3.6
Ramachandran plot (non-Gly, non-Pro residues)		
Most favored regions (%)	88.8	88.4
Additional allowed regions (%)	10.0	11.3
Generously allowed regions (%)	0.2	0.2
Disallowed regions (%)	0.1	0.1

*Values in parentheses are for the highest resolution shell. † $R_{sym} = \Sigma_h \Sigma_i |I_i(h) - \langle I(h) \rangle| / \Sigma_h \Sigma_i I_i(h)$, where $I_i(h)$ is the *i*th measurement. ‡The last shell R_{merge} for the high-resolution set is rather high because of the radiation damage in the later images. However, we include the data for the refinement because the refinement *R* factor and R_{free} for the shell are reasonably low, which indicates that the data in this shell are still useful for the refinement. §Phasing power is the rms value of F_h divided by the rms lack-of-closure error. ‖All the observed reflections are used for the refinement. ¶*R* factor $= \Sigma_h ||F(h)_{obs}| - |F(h)_{calc}|| / \Sigma_h |F(h)|$. #$R_{free}$ was calculated for 1% of reflections randomly excluded from the refinement.

the lack of a solvent connection. Instead, a proton is taken up from $His^{\gamma169}$ to O_1 and then menaquinol is released to the membrane. (iv) The deprotonated $His^{\gamma169}$ is very unstable, and this is immediately protonated through an extended water channel to $His^{\gamma169}$ after the release of menaquionol.

Proton motive force generation mechanism in the Fdh-N/Nar system. The Fdh-N structure, in combination of the Nar topology information, demonstrates that Fdh-N and Nar can form a redox loop where p.m.f. generation is best described as the sum of the following two effects (Fig. 1). (i) Two protons, which are taken up from the cytoplasm at the Fdh-N menaquinone reduction site, are translocated across the membrane and released to the periplasm from the menaquinol oxidation site in Nar. (ii) Two electrons are transferred from the formate oxidation site in periplasm to the NO_3^- reduction site in cytoplasm. This is not accompanied by an actual proton translocation across the membrane but generates a membrane potential, which is equivalent to $2H^+$ translocation across the membrane. The result is consistent with the measured ratio of proton translocation to electron transfer in this system (*6*).

References and Notes

1. For a review, see M. Saraste, *Science* **283**, 1488 (1999).
2. P. Mitchell, *J. Theor. Biol.* **62**, 327 (1976).
3. For a review, see B. C. Berks, S. J. Ferguson, J. W. Moir, D. J. Richardson, *Biochim. Biophys. Acta* **1232**, 97 (1995).
4. For a review, see D. J. Richardson, *Microbiology* **146**, 551 (2000).
5. For a review, see F. Blasco *et al.*, *Cell. Mol. Life Sci.* **58**, 179 (2001).
6. R. W. Jones, *FEBS Microbiol. Lett.* **8**, 167 (1980).
7. B. L. Berg, J. Li, J. Heider, V. Stewart, *J. Biol. Chem.* **266**, 22380 (1991).
8. Supplementary material is available on *Science* Online at www.sciencemag.org/cgi/content/295/5561/1863/DC1.
9. B. C. Berks *et al.*, *Mol. Microbiol.* **15**, 319 (1995).
10. S. Benoit, H. Abaibou, M. A. Mandrand-Berthelot, *J. Bacteriol.* **180**, 6625 (1998).
11. J. C. Boyington, V. N. Gladyshev, S. V. Khangulov, T. C. Stadtman, P. D. Sun, *Science* **275**, 1305 (1997).
12. C. C. Page, C. C. Moser, X. Chen, P. L. Dutton, *Nature* **402**, 47 (1999).
13. R. A. Rothery *et al.*, *J. Biol. Chem.* **273**, 7462 (1998).
14. For a review, see C. Kisker, H. Schindelin, D. C. Rees, *Annu. Rev. Biochem.* **66**, 233 (1997).
15. H. Schindelin, C. Kisker, J. Hilton, K. V. Rajagopalan, D. C. Rees, *Science* **272**, 1615 (1996).
16. J. M. Dias *et al.*, *Structure Fold. Design* **15**, 65 (1999).
17. T. A. Jones, J. Y. Zou, S. W. Cowan, M. Kjeldgaard, *Acta Crystallogr. Sect. A* **47**, 110 (1991).
18. S. V. Khangulov, V. N. Gladyshev, G. C. Dismukes, T. C. Stadtman, *Biochemistry* **37**, 3518 (1998).
19. L. C. Sieker, E. Adman, L. H. Jensen, *Nature* **235**, 40 (1972).
20. B. Guigliarelli *et al.*, *Eur. J. Biochem.* **207**, 61 (1992).
21. R. Gross, J. Simon, C. R. Lancaster, A. Kröger, *Mol. Microbiol.* **30**, 639 (1998).
22. L. Meek, D. J. Arp. *J. Bacteriol.* **182**, 3429 (2000).
23. A. Kröger, E. Winkler, A. Innerhofer, H. Hackenberg, H. Schägger, *Eur. J. Biochem.* **94**, 465 (1979).
24. S. Iwata *et al.*, *Science* **281**, 64 (1998).
25. C. R. Lancaster, A. Kröger, M. Auer, H. Michel, *Nature* **402**, 377 (1999).
26. S. Biel *et al.*, *Eur. J. Biochem.*, in press.
27. M. Jormakka, S. Törnroth, B. Byrne, S. Iwata, data not shown.
28. P. J. Kraulis, *J. Appl. Crystallogr.* **24**, 946 (1991).
29. R. Esnouf, *J. Mol. Graph.* **15**, 133 (1997).
30. E. A. Merritt, M. E. P. Murphy, *Acta Crystallogr. Sect. D* **50**, 869 (1994).

31. The research was supported by the Biotechnology and Biological Sciences Research Council of the UK and the Structural Biology Network of Sweden. We thank E. Mitchell and A. Thompson at the European Synchrotron Radiation Facility, Grenoble, for technical assistance J. Barber, B. C. Berks, R.C. Lancaster, F. Sargent, J. Butt, J. Simon, C. Page, and P. L. Dutton for critical assessment of this manuscript. The coordinates for the native Fdh-N and the HQNO complex are deposited with the PDB (entries 1KQF and 1KQG, respectively).

19 November 2001; accepted 14 January 2002

Evidence for Nuclear Emissions During Acoustic Cavitation

R. P. Taleyarkhan,[1]* C. D. West,[1]† J. S. Cho,[2] R. T. Lahey Jr.,[3] R. I. Nigmatulin,[4] R. C. Block[3]†

In cavitation experiments with deuterated acetone, tritium decay activity above background levels was detected. In addition, evidence for neutron emission near 2.5 million electron volts was also observed, as would be expected for deuterium-deuterium fusion. Control experiments with normal acetone did not result in tritium activity or neutron emissions. Hydrodynamic shock code simulations supported the observed data and indicated highly compressed, hot (10^6 to 10^7 kelvin) bubble implosion conditions, as required for nuclear fusion reactions.

The intense implosive collapse of gas or vapor bubbles, including acoustically forced cavitation bubbles, can lead to ultrahigh compressions and temperatures and to the generation of light flashes attributed to sonoluminescence (SL) (*1–21*). Our aim was to study ultrahigh compression and temperatures in bubbles nucleated by means of fast neutrons, whereby bubble nucleation centers with an initial radius R_0 of ~10 to 100 nm are created, and the bubbles grow in an acoustic field to a maximum radius (R_m) of ~ 1 mm (*19*) before an implosive collapse. This approach builds on the observations that (*17*) increasing R_m modestly (for example, by ~50%), or increasing the rate of collapse (*16*), can result in very large increases in peak gas temperatures and produce light emission during implosions. In contrast to single-bubble SL experiments, in which the initial bubble radius R_0 typically increases to R_m by a factor of only ~10 (for example, from ~10 μm to ~100 μm), our neutron-induced nucleation technique results in R_m/R_0 of ~10^5. For a spherical bubble, the increase of R_m/R_0 by a factor of 10^4 implies a related volumetric ratio increase of 10^{12} over that produced by conventional techniques. Our expectation was that such an approach, with its vastly increased energy concentration potential during implosions, should give rise to significant increases in the peak temperatures within the imploding bubbles, possibly leading to fusion and detectable levels of nuclear particle emissions in suitable fluids.

To minimize the effect of gas cushioning by promoting rapid condensation during implosive collapse, we elected to work with highly degassed organic liquids. An organic liquid was chosen [normal acetone (C_3H_6O) as the control fluid and deuterated acetone (C_3D_6O) as the test fluid] because it permitted the attainment of large tensile states without premature cavitation, and thus a lot of liquid superheat would be present before nucleation. Organic liquids also have relatively large phase change coefficients, which is important, as described later. Unless otherwise noted, the liquid in the chamber was maintained at ~0°C (which was the lowest value obtainable with the equipment we used). The test liquid was degassed and subjected to an acoustic pressure field that oscillated in resonance with the liquid sample and its container. The nucleation of vapor bubbles was initiated with fast neutrons from an isotopic source (Pu-Be) or from a pulsed neutron generator (PNG) that produces 14-MeV neutrons on demand at a predefined phase of the acoustic pressure field.

Experimental system. In the experimental apparatus (Fig. 1), the test liquid was placed in an approximately cylindrical glass flask and driven acoustically with a lead-zirconate-titanate (PZT) piezoelectric driver ring attached to the outer surface. Either a plastic or a liquid scintillation detector was used for detection of neutron and gamma signals (*22*). The light was detected and amplified in a photomultiplier tube (PMT). A

[1]Oak Ridge National Laboratory, Oak Ridge, TN 37831, USA. [2]Oak Ridge Associated Universities, Oak Ridge, TN 37830, USA. [3]Rensselaer Polytechnic Institute, Troy, NY 12180, USA. [4]Institute of Mechanics of Ufa–Bashkortostan Branch of the Russian Academy of Sciences, 6 Karl Marx Street, Ufa, 450 000, Russia.

*To whom correspondence should be addressed. E-mail: zrt@ornl.gov
†Retired.